applied sciences

MDPI

Article

Photocontrollable Mixed-Valent States in Platinum-Halide Ladder Compounds

Jun Ohara and Shoji Yamamoto *

Department of Physics, Hokkaido University, Sapporo 060-0810, Japan; ohara@phys.sci.hokudai.ac.jp
* Correspondence: yamamoto@phys.sci.hokudai.ac.jp; Tel.: +81-11-706-2681

Received: 6 October 2018; Accepted: 29 October 2018; Published: 2 November 2018

Abstract: Employing a two-orbital extended Peierls–Hubbard model, we demonstrate the photomanipulation of mixed-valent states in platinum-halide ladder compounds. There are two types of interchain valence arrangements, namely in-phase and out-of-phase types. The conversion of the in-phase structure to the out-of-phase structure is induced by photoirradiation, which is accelerated with increasing light intensity, while the reverse process hardly occurs. The out-of-phase arrangement is highly stabilized in the photoexcited states by the interchain electron transfer.

Keywords: photoinduced phase transition; halogen-bridged transition-metal complex; charge density wave; time-dependent Schrödinger equation

1. Introduction

Halogen (X)-bridged transition-metal (M) complexes (M = Pt, Pd, Ni; X = I, Br, Cl) are low-dimensional electron systems with chain [1–4], ladder [5,6], and prism structures [7,8], which present various quantum phases due to the interplay between electron–electron and electron–lattice interactions. For example, PtX chains exhibit the Peierls-distorted state $[\cdots X^{-}$–Pt^{4+}–$X^{-}\cdots Pt^{2+}\cdots]$ [9,10], while NiX chains show the Mott–Hubbard state $[-X^{-}-Ni^{3+}-X^{-}-Ni^{3+}-]$ [11,12]. Thus, we can tune the electronic structures by replacing constituent metals, halogens, and ligands. Applying pressure is another way of controlling electronic properties [13–15]. In the diplatinum-halide chain compounds [16–18], the pressure-induced phase transition between the charge-density-wave (CDW) state $[\cdots X^{-}-Pt^{3+}Pt^{3+}-X^{-}\cdots Pt^{2+}Pt^{2+}\cdots]$ and the charge-polarized (CP) state $[-X^{-}\cdots Pt^{2+}Pt^{3+}-X^{-}\cdots Pt^{2+}Pt^{3+}-]$ has been observed [19,20].

In addition to the chemical substitution and pressure application, dynamic control of electronic properties by photoirradiation has attracted much interest. The photoinduced phase transition between the Peierls-distorted and Mott–Hubbard states [21,22], and that between the CDW and CP states [23,24] have been reported. In such a global phase conversion, photogeneration of charge-transfer excitons (CTEs) [25] and following lattice relaxation are observed. In addition, photoinduced metalization has been observed in PtI chains [26], which occurs within 0.2 (ps). Thus, MX compounds may serve as ultrafast optical switching devices.

The platinum-halide ladder compound, which consists of two PtX chains connected with each other by interchain ligands (Figure 1), is a good model compound for the study of the interplay between photoinduced electron–phonon dynamics and lattice geometry. There are two types of MX ladder compounds with different interchain ligands: (μ-bpym)[Pt(en)X]$_2X$(ClO_4)$_3\cdot H_2O$ (X = Br, Cl; en = ethylendiamine = $C_2H_8N_2$; μ-bpym = 2,2′-bipyrimidine = $C_8H_6N_4$) and (bpy)[Pt(dien)Br]$_2Br_4\cdot 2H_2O$ (dien = diethylentriamine = $C_4H_{13}N_3$; bpy = 4,4′-bipyridyl = $C_{10}H_8N_2$) [5,6]. They show Pt^{2+}/Pt^{4+} valence-alternating ground states [27,28], where the interchain arrangement is in phase (IP) in the μ-bpym compounds, whereas it is out of phase (OP) in the bpy compounds. These competing CDWs can be optically distinguished from each other. Photoabsorption bands attributed to the intermetallic

charge-transfer excitations show single- and double-peaked structures in OP CDW and IP CDW, respectively [29]. A self-trapped exciton (STE) is photogenerated on the rung in IP CDW, whereas it is photogenerated on the leg in OP CDW [30,31]. Thus, the optical features of the ground and weakly-photoexcited states have been revealed. However, a study on the dynamics of photoinduced structural changes has so far been limited.

In this paper, we investigate the competition between IP CDW and OP CDW in the ground and photoexcited states with particular emphasis on the effects of the lattice geometry. In Section 2, we introduce a model Hamiltonian for *MX* ladder compounds. In Section 3, we reveal the ground-state properties of IP CDW and OP CDW. In Section 4, we investigate relaxation dynamics of the photoexcited CDWs by solving the time-dependent Schrödinger equation on one hand (Section 4.1) and calculating the adiabatic potential energy surfaces on the other hand (Section 4.2). Finally, we devote Section 5 to summary and discussion.

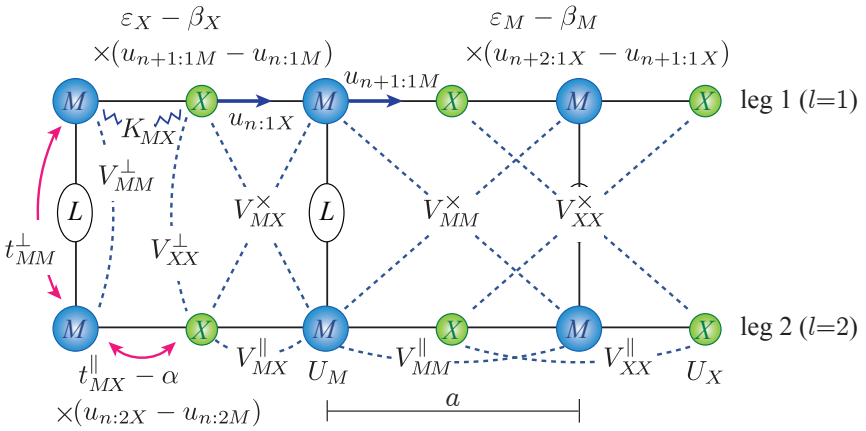

Figure 1. Modeling of *MX* ladder compounds. Metal, halogen, and interchain-ligand sites are denoted by *M*, *X*, and *L*, respectively. *a* is a lattice constant.

2. Modeling

To describe *MX* ladder compounds (Figure 1), we employ the two-orbital extended Peierls–Hubbard Hamiltonian

$$\mathcal{H} = \mathcal{H}_{\rm el} + \mathcal{H}_{\rm lat} + \mathcal{H}_{\rm el-lat}: \tag{1}$$

$$\begin{aligned}\mathcal{H}_{\rm el} &= -\sum_{n,l,s}\left(t^{\parallel}_{MX}c^{\dagger}_{n+1:lMs}c_{n:lXs} + t^{\parallel}_{MX}c^{\dagger}_{n:lXs}c_{n:lMs} + \tfrac{t^{\perp}_{MM}}{2}c^{\dagger}_{n:l+1Ms}c_{n:lMs} + {\rm H.c.}\right)\\ &+\sum_{n,l,s}\left(\varepsilon_M n_{n:lMs} + \varepsilon_X n_{n:lXs}\right) + \sum_{n,l,s,s'}\left\{\sum_{A=M,X}\tfrac{U_A}{2}n_{n:lAs}n_{n:lAs'}\delta_{s,-s'}\right.\\ &+V^{\parallel}_{MX}(n_{n+1:lMs}+n_{n:lMs})n_{n:lXs'} + V^{\times}_{MX}(n_{n+1:lMs}+n_{n:lMs})n_{n:3-lXs'}\\ &\left.+\sum_{A=M,X}\left(V^{\parallel}_{AA}n_{n+1:lAs}n_{n:lAs'} + \tfrac{V^{\perp}_{AA}}{2}n_{n:lAs}n_{n:3-lAs'} + V^{\times}_{AA}n_{n+1:lAs}n_{n:3-lAs'}\right)\right\},\end{aligned} \tag{2}$$

$$\mathcal{H}_{\rm lat} = \sum_{n,l}\left\{\tfrac{K_{MX}}{2}\left[(u_{n:lX}-u_{n:lM})^2 + (u_{n+1:lM}-u_{n:lX})^2\right] + \tfrac{M_M}{2}\dot{u}^2_{n:lM} + \tfrac{M_X}{2}\dot{u}^2_{n:lX}\right\}, \tag{3}$$

$$\begin{aligned}\mathcal{H}_{\rm el-lat} &= -\sum_{n,l,s}\left[\alpha(u_{n:lX}-u_{n+1:lM})c^{\dagger}_{n+1:lMs}c_{n:lXs} - \alpha(u_{n:lX}-u_{n:lM})c^{\dagger}_{n:lXs}c_{n:lMs} + {\rm H.c.}\right]\\ &-\sum_{n,l,s}\left[\beta_M(u_{n:lX}-u_{n-1:lX})n_{n:lMs} + \beta_X(u_{n+1:lM}-u_{n:lM})n_{n:lXs}\right].\end{aligned} \tag{4}$$

$\mathcal{H}_{\rm el}$ denotes the electronic part of the total Hamiltonian in the second-quantization representation, where $n_{n:lAs}$ $(= c^{\dagger}_{n:lAs}c_{n:lAs})$ is a number operator of an s $(=\uparrow,\downarrow=+,-)$-spin electron at site A $(=M,X)$ on leg l $(=1,2)$ and unit n $(=1,\cdots,N)$. N is a total number of units. We consider half-filled d_{z^2} orbitals on metal (M) ions and fully-filled p_z orbitals on halogen (X) ions, where ε_A $(A=M,X)$ denotes the orbital energy of the isolated ion. The intrachain and interchain transfer integrals are denoted by $t^{\parallel}_{MX}$ and $t^{\perp}_{MM}$, respectively. The on-site and intersite Coulomb repulsions are modeled by U_A $(A=M,X)$ and $V^{\parallel,\perp,\times}_{AA'}$ $(A,A'=M,X)$, respectively. $\mathcal{H}_{\rm lat}$ describes the elastic and kinetic energies of a lattice system, where leg-direction displacement and the mass of the metal (halogen) ion are denoted by $u_{n:lM(X)}$ and $M_{M(X)}$, respectively. K_{MX} is a spring constant. In the present paper, the lattice displacement $u_{n:lM(X)}$ is treated as a classical value [32–34]. $\mathcal{H}_{\rm el-lat}$ represents electron–lattice interactions, which contain Peierls (α) and Holstein (β_M, β_X) type couplings.

The intrachain transfer integral and the spring constant are taken as $t^{\parallel}_{MX}=1.54$ (eV) and $K^{\parallel}_{MX}=6.00$ (eVÅ^{-2}), respectively [1,2]. The values of the Coulomb parameters and the electron–lattice couplings are as follows, $U_M/t^{\parallel}_{MX}=U_X/t^{\parallel}_{MX}=1.00$, $V^{\parallel}_{MX}/t^{\parallel}_{MX}=0.35$, $V^{\times}_{MX}/t^{\parallel}_{MX}=0.13$, $V^{\parallel}_{MM}/t^{\parallel}_{MX}=0.15$, $V^{\parallel}_{XX}/t^{\parallel}_{MX}=V^{\perp}_{XX}/t^{\parallel}_{MX}=V^{\times}_{XX}/t^{\parallel}_{MX}=0.10$, and $\beta_M/\sqrt{K_{MX}t^{\parallel}_{MX}}=\beta_X/\sqrt{K_{MX}t^{\parallel}_{MX}}=3\alpha/\sqrt{K_{MX}t^{\parallel}_{MX}}=0.75$. The orbital energy is taken as $(\varepsilon_M-\varepsilon_X)/t^{\parallel}_{MX}=1.50$. These parameter values are based on a theoretical consideration in the previous work [29], which revealed the ground-state optical properties of MX ladder compounds by employing the d-p-π model. Under these parameterizations, the present model can also reproduce the observed optical gaps 2.5∼3.5 (eV) [29] (see Figure 2c). The Coulomb interactions are treated within a Hartree-Fock (HF) approximation.

3. Competing Mixed-Valent States and Their Optical Properties

Various possible electronic states of the MX ladders were revealed through a group-theoretical analysis [27]. When $M=$ Pt, electron–lattice couplings cause dimerization of the halogen sublattice, which is accompanied by a CDW on the metal sublattice. The interchain valence arrangement is either IP or OP, as shown in Figure 2a. In the strong-coupling limit, we have a difference in energy between OP CDW and IP CDW within the single-band approximation [29],

$$\frac{E_{\rm OP}-E_{\rm IP}}{N}=2(2V^{\times}_{MM}-V^{\perp}_{MM})-\frac{2\left(t^{\perp}_{MM}\right)^2}{4\beta_M u-U_M+V^{\perp}_{MM}+4(V^{\parallel}_{MM}-V^{\times}_{MM})}, \tag{5}$$

where the energy gain by the interchain electron hopping is taken into account within the second-order perturbation scheme, while $u\equiv|u_{n:lX}-u_{n:lM}|=|u_{n+1:lM}-u_{n:lX}|$ indicates the bond variable in isolated MX chains. The first term on the right-hand side of Equation (5) corresponds to the naivest Coulomb energy difference between OP CDW and IP CDW. In the absence of Coulomb interactions, the energy of OP CDW is always lower than that of IP CDW by the energy gain $\propto(t^{\perp}_{MM})^2$. Figure 2b shows ground-state phase diagrams of the present model [Equation (1)] in the moderate-coupling regime at the sufficiently low temperature $k_{\rm B}T/t^{\parallel}_{MX}=0.001$, which are numerically obtained. The lattice displacements are adiabatically treated and numerically determined to minimize free energy. Considering that Coulomb force depends on electron–electron distance in general, the condition $V^{\perp}_{MM}>V^{\times}_{MM}$ is suitable for the lattice structure. The obtained phase boundaries are in this region and agree well with the above simple calculation Equation (5).

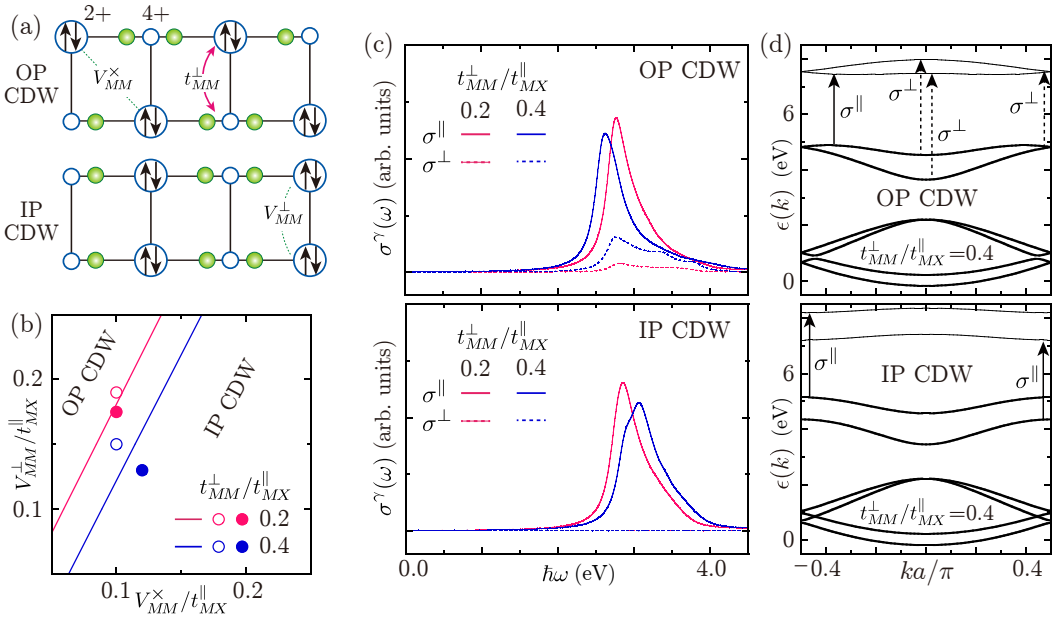

Figure 2. (**a**) Schematic representations of OP CDW and IP CDW. (**b**) Ground-state phase diagrams on the $V^{\times}_{MM}$-$V^{\perp}_{MM}$ plane, where two sets of parameterization are shown by different colors. The symbols • and ○ indicate the IP-CDW and OP-CDW initial states, respectively, in the investigation of photoinduced dynamics. (**c**) Polarized optical conductivity spectra of the CDW states. (**d**) Dispersion relations of the CDW states at $t^{\perp}_{MM}/t^{\parallel}_{MX} = 0.4$. Conduction and valence bands are shown by thin and thick lines, respectively, and up- and down-spin electron bands are degenerate.

Let us observe polarized optical conductivity spectra of the IP-CDW and OP-CDW ground states,

$$\sigma^{\gamma}(\omega) = \frac{\pi}{N\omega}\sum_{\lambda}|\langle E_{\lambda}|\mathcal{J}^{\gamma}|E_0\rangle|^2\delta(E_{\lambda}-E_0-\hbar\omega). \tag{6}$$

$|E_{\lambda}\rangle$ is a one-electron–hole pair excited state from $|E_0\rangle$ corresponding to either OP CDW or IP CDW, and the current-density operators parallel ($\gamma = \parallel$) and perpendicular ($\gamma = \perp$) to the leg direction are defined by

$$\begin{aligned}\mathcal{J}^{\parallel} &= \tfrac{i\bar{a}e}{\hbar}\sum_{n,l,s}\Big\{[t^{\parallel}_{MX}+\alpha(u_{n:lX}-u_{n+1:lM})]c^{\dagger}_{n+1:lMs}c_{n:lXs} \\ &\quad +[t^{\parallel}_{MX}-\alpha(u_{n:lX}-u_{n:lM})]c^{\dagger}_{n:lXs}c_{n:lMs}-\text{H.c.}\Big\},\end{aligned} \tag{7}$$

$$\mathcal{J}^{\perp} = \tfrac{ice}{\hbar}\sum_{n,s}(t^{\perp}_{MM}c^{\dagger}_{n:2Ms}c_{n:1Ms}-\text{H.c.}), \tag{8}$$

where the M–X distance along the leg and the M-M one along the rung are taken as $\bar{a} = a/2$ and $c = a$, respectively.

In Figure 2c, $\sigma^{\parallel}$ shows a single-peaked structure in OP CDW at each $t^{\perp}_{MM}$, whereas it shows a shoulder-like one in IP CDW at $t^{\perp}_{MM}/t^{\parallel}_{MX} = 0.4$. In OP CDW, an electron transition from the highest-occupied molecular orbital (HOMO) to the lowest-unoccupied molecular orbital (LUMO) contributes to the major optical absorption (see the solid arrow in the upper panel of Figure 2d). In IP CDW, on the other hand, a HOMO-to-LUMO electron transition is optically forbidden and another two excitation modes predominantly contribute to the optical absorption (see solid arrows in the lower panel of Figure 2d). These transition energies are different from each other due to electron–hole symmetry breaking [29], which becomes obvious with increasing $t^{\perp}_{MM}$. $\sigma^{\perp}$ is significantly affected by an interchain valence arrangement. In IP CDW, $\sigma^{\perp}$ shows no absorption because electrons on metal ions have no chance of hopping along the rung. In the OP-type valence arrangement, such an electron transfer is possible and the resultant absorption is observed. The electron excitations at the zone center

and at the zone boundary make a large contribution to $\sigma^{\perp}$ (see dotted arrows in Figure 2d). However, the total oscillator strength of $\sigma^{\perp}$ is smaller than that of $\sigma^{\parallel}$ due to the situation $t^{\perp}_{MM} < t^{\parallel}_{MX}$.

4. Photoexcitation and Following Lattice Relaxation

We focus on the IP-CDW and OP-CDW ground states in the vicinity of the phase boundaries (see Figure 2b), and reveal whether and how IP CDW and OP CDW are manipulated by photoirradiation. Since both the CDWs are less active against the incident light perpendicular to the leg direction as discussed above, we consider the leg-direction-polarized photoirradiation, where the photon energies are tuned to the optical gaps.

4.1. Real-Time Dynamics

Electron and lattice dynamics of photoexcited MX ladders is investigated by solving the time-dependent Schrödinger equation

$$i\hbar\frac{\mathrm{d}}{\mathrm{d}t}|\psi_{\nu,s}(t)\rangle = \mathcal{H}_{\mathrm{HF}}(t)|\psi_{\nu,s}(t)\rangle, \tag{9}$$

where $|\psi_{\nu,s}(t)\rangle$ $(\nu = 1, \cdots, 4N; s = +, -)$ is the one-particle wave function for the s-spin electron on the νth energy level, which at $t \to -\infty$ corresponds to the νth eigenstate of the static HF Hamiltonian [35,36]. We consider photoirradiation of the system by multiplying an electron-hopping term by a Peierls phase factor [37],

$$c^{\dagger}_{n:lMs}c_{n':lXs} \to \exp\left[i\frac{e}{\hbar v}\boldsymbol{A}(t)\cdot(\boldsymbol{r}_{n:lM} - \boldsymbol{r}_{n':lX})\right]c^{\dagger}_{n:lMs}c_{n':lXs}, \tag{10}$$

where v is the speed of light and $\boldsymbol{r}_{n:lM(X)}$ is the position vector of a metal (halogen) ion, while a pumping laser pulse is described by the vector potential

$$\boldsymbol{A}(t) = \boldsymbol{A}_0 e^{-\gamma^2 t^2}\cos\omega_0 t \tag{11}$$

with the photon energy $\hbar\omega_0$ and the pulse width γ^{-1}. We consider the leg-direction-polarized light $\boldsymbol{A}_0 = (A_0\hbar v/e\bar{a}, 0)$, where A_0 is the dimensionless amplitude of the vector potential, and set γ^{-1} equal to 0.04 (ps). Time evolution of the lattice displacement $u_{n:lA}$ $(A = M, X)$ is determined by the equation of motion

$$M_A\frac{\mathrm{d}^2}{\mathrm{d}t^2}u_{n:lA}(t) = -\frac{\partial\langle\mathcal{H}_{\mathrm{HF}}(t)\rangle}{\partial u_{n:lA}(t)}\Big[\equiv F_A(t)\Big], \tag{12}$$

where $\langle\cdots\rangle$ means an expectation value in the state $|\Psi(t)\rangle = \Pi_{\nu=1}^{3N}\otimes|\psi_{\nu,+}(t)\rangle|\psi_{\nu,-}(t)\rangle$. $|\Psi(-\infty)\rangle$ corresponds to the initial CDW state. Discretizing the time by Δt, we numerically integrate Equations (9) and (12) step by step. The numerical algorithm consists of the following steps. Firstly, we obtain

$$\begin{aligned}|\psi_{\nu,s}(t+\Delta t)\rangle &= T\exp\left[-\tfrac{i}{\hbar}\int_t^{t+\Delta t}\mathrm{d}t'\mathcal{H}_{\mathrm{HF}}(t')\right]|\psi_{\nu,s}(t)\rangle\\ &\simeq \exp\left[-\tfrac{i\mathcal{H}_{\mathrm{HF}}(t)}{\hbar}\Delta t\right]|\psi_{\nu,s}(t)\rangle\\ &= \sum_{\lambda=1}^{4N}\sum_{\tau}\exp\left[-\tfrac{i\tilde{\epsilon}_{\lambda,\tau}}{\hbar}\Delta t\right]|\tilde{\phi}_{\lambda,\tau}\rangle\langle\tilde{\phi}_{\lambda,\tau}|\psi_{\nu,s}(t)\rangle,\end{aligned} \tag{13}$$

where T is the time-ordering operator, while $\tilde{\epsilon}_{\lambda,\tau}$ and $|\tilde{\phi}_{\lambda,\tau}\rangle$ are the eigenvalue and the eigenfunction of the instantaneous Hamiltonian $\mathcal{H}_{\mathrm{HF}}(t)$, respectively. Here, we note that

$$\sum_{\lambda=1}^{4N}\sum_{\tau}|\tilde{\phi}_{\lambda,\tau}\rangle\langle\tilde{\phi}_{\lambda,\tau}| = 1. \tag{14}$$

The lattice part is solved as

$$u_{n:lA}(t+\Delta t) = u_{n:lA}(t) + \dot{u}_{n:lA}(t)\Delta t, \tag{15}$$

$$\dot{u}_{n:lA}(t+\Delta t) = \dot{u}_{n:lA}(t) + \frac{F_A(t)}{M_A}\Delta t. \tag{16}$$

Thus, we obtain the electronic wavefunctions and the lattice displacements at $t+\Delta t$, which are correct up to $\mathcal{O}(\Delta t)$. We can estimate $\mathcal{H}_{\rm HF}(t+\Delta t)$ from $\{|\psi_{\nu,s}(t+\Delta t)\rangle\}$, $\{u_{n:lA}(t+\Delta t)\}$, and $\{\dot{u}_{n:lA}(t+\Delta t)\}$. Secondly, we construct the instantaneous Hamiltonian at $t+\Delta t/2$ as

$$\mathcal{H}_{\rm HF}(t+\frac{\Delta t}{2}) \equiv \frac{1}{2}\left[\mathcal{H}_{\rm HF}(t) + \mathcal{H}_{\rm HF}(t+\Delta t)\right], \tag{17}$$

and the force at $t+\Delta t/2$ as

$$F_A(t+\frac{\Delta t}{2}) \equiv \frac{1}{2}\left[F_A(t) + F_A(t+\Delta t)\right]. \tag{18}$$

The lattice displacements and velocities at $t+\Delta t/2$ are estimated as

$$u_{n:lA}(t+\frac{\Delta t}{2}) = u_{n:lA}(t) + \dot{u}_{n:lA}(t)\frac{\Delta t}{2}, \tag{19}$$

$$\dot{u}_{n:lA}(t+\frac{\Delta t}{2}) = \dot{u}_{n:lA}(t) + \frac{F_A(t)}{M_A}\frac{\Delta t}{2}, \tag{20}$$

which are obtained by $\Delta t \to \Delta t/2$ in Equations (15) and (16). Finally, we update the electronic wavefunctions and the lattice displacements by using the information at $t+\Delta t/2$: $\mathcal{H}_{\rm HF}(t) \to \mathcal{H}_{\rm HF}(t+\Delta t/2)$ in Equation (13), $\dot{u}_{n:lA}(t) \to \dot{u}_{n:lA}(t+\Delta t/2)$ in Equation (15), and $F_A(t) \to F_A(t+\Delta t/2)$ in Equation (20). Thus, the wavefunctions are represented as

$$\begin{aligned} |\psi_{\nu,s}(t+\Delta t)\rangle &\simeq \exp\left[-\tfrac{i\mathcal{H}_{\rm HF}(t+\Delta t/2)}{\hbar}\Delta t\right]|\psi_{\nu,s}(t)\rangle \\ &= \sum_{\lambda=1}^{4N}\sum_{\tau}\exp\left[-\tfrac{i\epsilon_{\lambda,\tau}}{\hbar}\Delta t\right]|\phi_{\lambda,\tau}\rangle\langle\phi_{\lambda,\tau}|\psi_{\nu,s}(t)\rangle, \end{aligned} \tag{21}$$

where $\epsilon_{\lambda,\tau}$ and $|\phi_{\lambda,\tau}\rangle$ are the eigenvalue and the eigenfunction of $\mathcal{H}_{\rm HF}(t+\Delta t/2)$, respectively. The lattice displacements are given by the following set of equations:

$$u_{n:lA}(t+\Delta t) = u_{n:lA}(t) + \dot{u}_{n:lA}(t+\frac{\Delta t}{2})\Delta t, \tag{22}$$

$$\dot{u}_{n:lA}(t+\frac{\Delta t}{2}) = \dot{u}_{n:lA}(t) + \frac{F_A(t+\Delta t/2)}{M_A}\frac{\Delta t}{2}. \tag{23}$$

The thus obtained solutions Equations (21) and (22) are correct up to $\mathcal{O}(\Delta t^2)$ [36,38,39]. The optical phonon frequency $\omega_{\rm ph}$ is given by $\omega_{\rm ph} = \sqrt{2K_{MX}/M_{\rm eff}}$ with the effective mass $M_{\rm eff} = M_M M_X/(M_M + M_X) = 4.9 \times 10^{-26}$ (kg). The time interval is taken as $\Delta t = 5.0 \times 10^{-4}\omega_{\rm ph}^{-1} = 7.6 \times 10^{-3}$ (fs). We confirmed that the total energy of the system after turnoff of the pumping conserves within 2×10^{-3} percent in the numerical simulations. We note that the electronic wavefunction $|\psi_{\nu,s}(t)\rangle$ deviates from the eigenstates of the instantaneous Hamiltonian, as shown in Equation (21). In the simulations, the kinetic-energy part in Equation (3) serves as a heat bath and therefore the photoexcited electronic system can be relaxed. Thus, the electron system and the classical lattice system are simultaneously updated. The similar methods are applied to electron–spin coupled systems [40] as well, where local spins coupled with conducting electrons are treated classically. We initially add small random values to the lattice displacements as thermal fluctuations, which are three orders of magnitude smaller than

the initial lattice displacements [41]. Hereafter, the total number of units N is set equal to 64, unless otherwise noticed.

To observe photoinduced structural changes, we calculate the electron density on the platinum sublattice

$$d_{n:l}(t) = \sum_s \langle c^\dagger_{n:lMs} c_{n:lMs} \rangle \tag{24}$$

and its alternating component defined as

$$\tilde{d}_{n:l}(t) = \frac{(-1)^n}{4} \Big[d_{n-1:l}(t) - 2d_{n:l}(t) + d_{n+1:l}(t) \Big]. \tag{25}$$

We can distinguish the IP-CDW domain from the OP-CDW one by observing the order parameter

$$O_n(t) = \frac{\tilde{d}_{n:1}(t)\tilde{d}_{n:2}(t)}{\sqrt{|\tilde{d}_{n:1}(t)\tilde{d}_{n:2}(t)|}}. \tag{26}$$

$O_n(t)$ takes positive and negative values for the IP and OP configurations, respectively. In addition, we estimate the absorbed photon density

$$n_{\rm ph} = \frac{1}{4N} \frac{\langle \mathcal{H}_{\rm HF}(t = 2.9{\rm ps}) \rangle - \langle \mathcal{H}_{\rm HF}(-\infty) \rangle}{\hbar\omega_0}, \tag{27}$$

which indicates the effective intensity of pumping light. It monotonically increases with increasing A_0.

Figure 3 shows time evolution of the photoexcited IP CDW and OP CDW. On the IP-CDW background at $t^\perp_{MM}/t^\parallel_{MX} = 0.2$ (Figure 3a), local deformations are generated at around $n = 8$, 18, and 40 after photoirradiation, which correspond to STEs [42,43]. The defect at $n = 40$ dissociates into solitons [44–47], while the others just disappear. The solitonic excitation generates a stable antiphase CDW domain on the leg-1 chain. The IP-type charge-ordering pattern is thus photoconverted into the OP-type one. On the OP-CDW background at $t^\perp_{MM}/t^\parallel_{MX} = 0.2$ (Figure 3b), on the other hand, a local deformation appears at around $n = 38$ on the leg-2 chain after photoirradiation but it disappears soon. There occurs no phase conversion. Figure 4a shows the case of the IP-CDW background at $t^\perp_{MM}/t^\parallel_{MX} = 0.4$. Although the absorbed photon density is almost the same as the case of $t^\perp_{MM}/t^\parallel_{MX} = 0.2$, many soliton pairs appear. An interchain arrangement of the antiphase CDW domains becomes "out of phase" as time passes, which leads to the global phase conversion. On the OP-CDW background at $t^\perp_{MM}/t^\parallel_{MX} = 0.4$ (Figure 4b), on the other hand, several antiphase CDW domains are photoinduced but they do not contribute to the OP-to-IP phase conversion at all. An interchain arrangement of these domains is "in phase" and therefore there is no phase transition. This relaxation process reads as the formation of an antiphase OP-CDW ($\overline{\rm OP}$) structure.

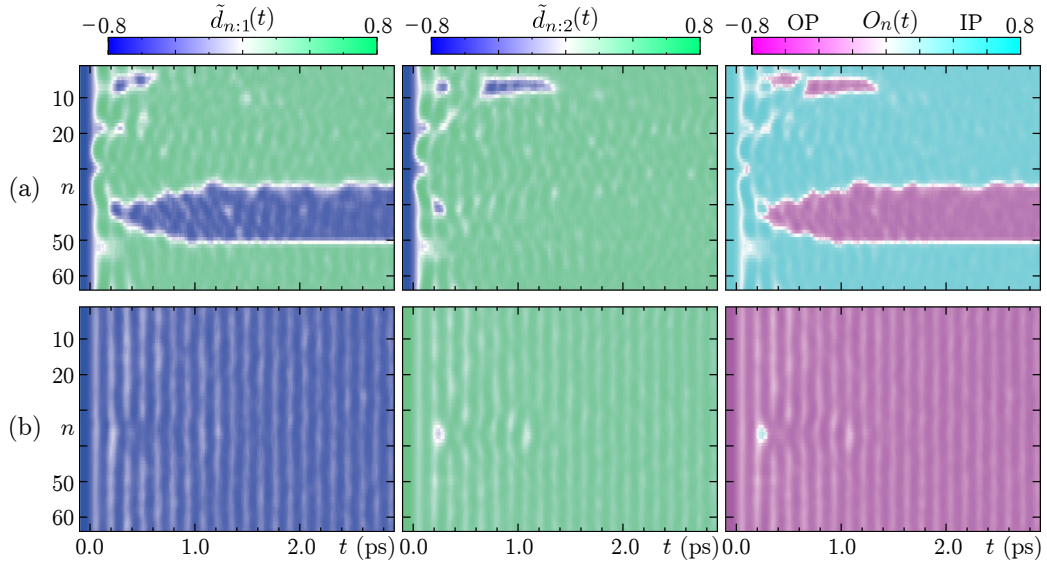

Figure 3. Photoinduced charge dynamics on the IP-CDW background at $t^{\perp}_{MM}/t^{\parallel}_{MX} = 0.2$ with $A_0 = 0.04$ ($n_{\rm ph} = 0.08$) (**a**) and on the OP-CDW background at $t^{\perp}_{MM}/t^{\parallel}_{MX} = 0.2$ with $A_0 = 0.03$ ($n_{\rm ph} = 0.09$) (**b**): the CDW amplitude on each leg $\tilde{d}_{n:l}(t)$ ($l = 1, 2$) and the order parameter $O_n(t)$ are presented.

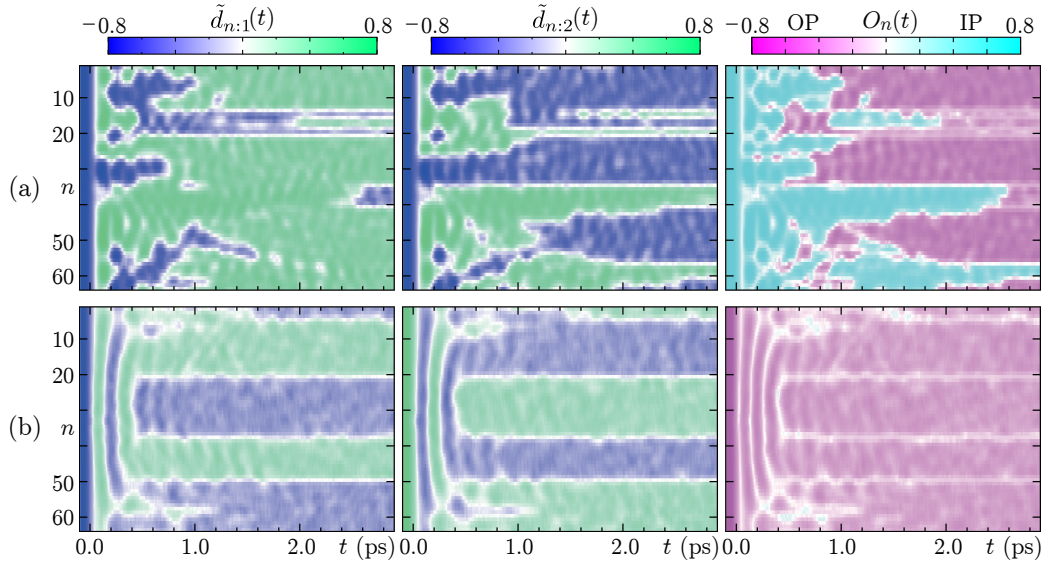

Figure 4. The same as Figure 3 on the IP-CDW background at $t^{\perp}_{MM}/t^{\parallel}_{MX} = 0.4$ with $A_0 = 0.02$ ($n_{\rm ph} = 0.07$) (**a**) and on the OP-CDW background at $t^{\perp}_{MM}/t^{\parallel}_{MX} = 0.4$ with $A_0 = 0.05$ ($n_{\rm ph} = 0.10$) (**b**).

We here reveal light intensity dependences of the relaxation dynamics. Figure 5a–d presents OP- and IP-domain ratios,

$$R_{\rm OP}(t) = \frac{1}{2N}\sum_{n=1}^{N}\left(1 - \frac{O_n(t)}{|O_n(t)|}\right), \tag{28}$$

$$R_{\rm IP}(t) = \frac{1}{2N}\sum_{n=1}^{N}\left(1 + \frac{O_n(t)}{|O_n(t)|}\right), \tag{29}$$

and normalized CDW amplitude,

$$R_{\mathrm{CO}}(t) = \frac{\sum_{n=1}^{N} \sqrt{|\tilde{d}_{n:1}(t)\tilde{d}_{n:2}(t)|}}{\sum_{n=1}^{N} \sqrt{|\tilde{d}_{n:1}(-\infty)\tilde{d}_{n:2}(-\infty)|}}, \tag{30}$$

as functions of n_{ph}. In both CDWs, charge ordering is weakened with increasing n_{ph}. This is not surprising given that photon absorption reads as the charge-transfer excitation. We suppose that the CDW order is melted at around n_{ph} = 0.11–0.14 (a photon per 7–9 sites), where R_{CO} becomes less than 0.2 (shaded regions in Figure 5a–d). We focus on the CDW region. The naivest photoconversion processes by the charge-transfer excitations are illustrated in Figure 5e. These processes are expressed by the relation R (a conversion rate)$= 4n_{\mathrm{ph}}$ (an absorbed-photon number per unit). On the IP-CDW background (Figure 5a,b), a weak photoexcitation can never induce the phase conversion. Once n_{ph} exceeds a threshold value, however, the conversion rate R_{OP} increases beyond R. This can be regarded as a cooperative structural change due to a domino effect [48,49]. Thus, the phase conversion is nonlinearly accelerated with increasing n_{ph}, which is particularly pronounced in the strongly-coupled chains (Figure 5b). On the OP-CDW background (Figure 5c,d), on the other hand, the OP-to-IP phase conversion is never observed over the whole range of n_{ph}.

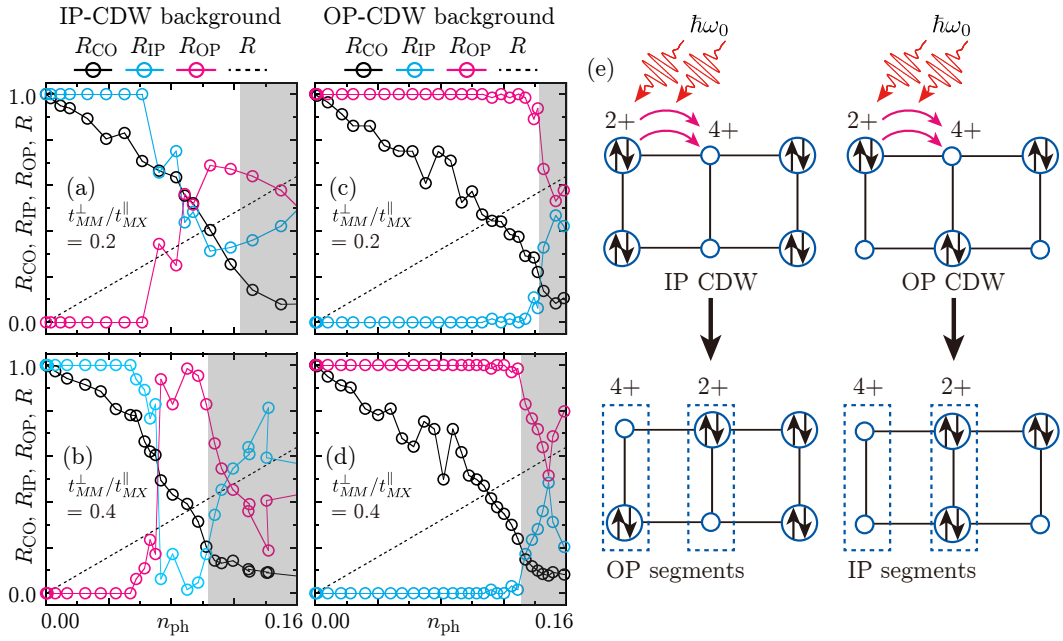

Figure 5. Light intensity dependences of photoinduced charge dynamics on the IP-CDW backgrounds at $t_{MM}^{\perp}/t_{MX}^{\parallel} = 0.2$ (**a**) and 0.4 (**b**), and on the OP-CDW backgrounds at $t_{MM}^{\perp}/t_{MX}^{\parallel} = 0.2$ (**c**) and 0.4 (**d**): the normalized CDW amplitude R_{CO}, the IP-CDW ratio R_{IP}, and the OP-CDW ratio R_{OP} at $t = 2.9$ (ps) are presented as functions of n_{ph}. The conversion ratio $R = 4n_{\mathrm{ph}}$ represents the naivest photoconversion processes (**e**).

A decrease in the CDW amplitude shown in Figure 5 results in a decrease in the Coulomb energy difference between IP CDW and OP CDW in Equation (5). In such a situation, the interchain coupling $t_{MM}^{\perp}$, which favors the OP arrangement, may become a more decisive factor in the phase competition. Therefore, in the photoexcited MX ladders, the OP-type valance arrangement is highly stable compared to the IP-type one.

4.2. Variational Calculation

We take a variational approach to lattice dynamics [42,50] and reveal the stabilization of the OP-CDW configuration in photoexcited states. Any conversion between IP CDW and OP CDW is caused by emergent solitons in pairs. To describe the relaxation channels via soliton pairs, we introduce bond variables,

$$u^{-}_{n:l} \equiv u_{n:lX} - u_{n:lM}, \tag{31}$$

$$u^{+}_{n:l} \equiv u_{n+1:lM} - u_{n:lX}, \tag{32}$$

and define a trial wavefunction,

$$u^{\pm}_{n:l} = \pm(-1)^n u_l s_{n:l} \quad (l = 1, 2); \tag{33}$$

$$s_{n:l} = \left[1 + \kappa_l \left\{ \tanh \frac{|n - N/2| - d_l/2}{\xi_l} - 1 \right\}\right], \tag{34}$$

where u_l ($l = 1, 2$) is the initial CDW amplitude, κ_l and ξ_l are variational parameters to design each soliton defect, and d_l denotes their distance along the legs. We set d_1 and d_2 equal to d for simplicity. The n-photon excited state from the static HF state $|E_0\rangle$ described by Equation (33) is given as

$$|E_{\rm ex}\rangle \equiv \prod_{i=1}^{n} \tilde{c}^{\dagger}_{\nu_i,\tau_i} \tilde{c}_{\mu_i,\tau_i} |E_0\rangle, \tag{35}$$

where $\tilde{c}^{\dagger}_{\nu_i,\tau_i}$ creates the τ_i-spin electron of the ν_ith HF-level energy ϵ_{ν_i,τ_i}, while the indices satisfy the condition $\epsilon_{\mu_i,\tau_i} \leq \epsilon_{\rm F}$ (Fermi energy) $< \epsilon_{\nu_i,\tau_i}$ and n electron–hole pairs are selected in ascending order of their creation energies $\epsilon_{\nu_i,s_i} - \epsilon_{\mu_i,s_i}$. The variational parameters are determined to minimize the photoexcited-state energy $E_{\rm ex} = \langle E_{\rm ex}|\mathcal{H}_{\rm HF}|E_{\rm ex}\rangle$ at every d, where $\mathcal{H}_{\rm HF}$ is the static HF Hamiltonian. An energy of the excited state immediately after photoexcitation ($\kappa_1 = \kappa_2 = d = 0$) is denoted by $E^0_{\rm ex}$. In the calculation, the lattice displacements are treated adiabatically. In other words, the kinetic-energy part in Equation (3) is discarded.

The thus calculated adiabatic potential energy surfaces of the n-photon excited states are presented in Figure 6a–c. The optimized $\boldsymbol{\kappa} = (\kappa_1, \kappa_2)$ at $d = 0$ and 16 are plotted in Figure 6a′–c′, where the situation $\kappa_1 \geq \kappa_2$ is focused on because the energy surfaces are symmetric with respect to the line $\kappa_1 = \kappa_2$. In the case of $n = 1$ (Figure 6a,a′), the photogenerated CTE begins to be localized with increasing κ_l while keeping $d = 0$. In IP CDW, the local deformation appears on each chain ($\kappa_1 = \kappa_2 \neq 0$ at $d = 0$). In OP CDW, on the other hand, it appears on either one of the two chains ($\kappa_1 \neq 0$, $\kappa_2 = 0$ at $d = 0$). These results are consistent with the d-p-π model calculations [31]. With increasing d, the photoexcited-state energies increase with diminishing κ_l. The local defect at $d = 0$ cannot dissociate into a soliton pair in each CDW. In the case of $n = 4$ (Figure 6b,b′), the situation is almost the same. On both the CDW backgrounds, four CTEs can be merged into a local defect described by the finite κ_l at $d = 0$ but global structural changes are never induced. This relaxation dynamics induced by the weak photoexcitation is observed in Figure 3a,b as disappearance of the photoinduced defects. The time-evolutional calculations reveal geminate recombination of solitons (Figure 3a) and background charge oscillations (Figure 3a,b). This dynamics is hard to see within this variational approximation.

The situation is drastically changed in the case of $n = 8$ (Figure 6c,c′), where the IP-to-OP phase conversion is possible but the reverse process never occurs. Self-trapping of CTEs is observed on each CDW background as with the one- and four-photon excitation cases. In the IP backgrounds, the thus formed local defect can dissociate into a pair of two distant solitons on a chain, while CDW on the adjacent chain is just weakened ($\kappa_1 \simeq 1 \gg \kappa_2$ at $d = 16$). This is the photogeneration of the OP structure. In the OP backgrounds, on the other hand, a soliton pair is formed on each chain ($\kappa_1 = \kappa_2 \simeq 1$ at $d = 16$), which reads as the photogeneration of the $\overline{\rm OP}$ structure. The OP-type valence arrangement

is energetically more stable than the IP-type one in the strongly-photoexcited states. Thus, we obtain qualitatively the same light intensity dependence as in Figure 5. We focus on photoirradiation of the IP-CDW ground state and compare the energy of the photoinduced OP-CDW configuration $E_{\rm ex}(d = N)$ with that of the IP-CDW configuration $E^0_{\rm ex}$. Figure 7a presents the thus obtained boundaries between OP CDW and IP CDW in the photoexcited *MX* ladders. Since an OP-CDW region is extended by the photoexcitation, the IP-CDW ground state in the vicinity of the phase boundary can be photoconverted. On the other hand, the IP CDW far away from the phase boundary never shows the cooperative structural change, as shown in Figure 7b.

The multi-photon excitation is necessary for the occurrence of the phase conversion. Such a threshold behavior in uncorrelated coupled chains has been pointed out [50]. The *MX* ladder systems with relevant Coulomb correlations possibly show the photoinduced directional phase transition.

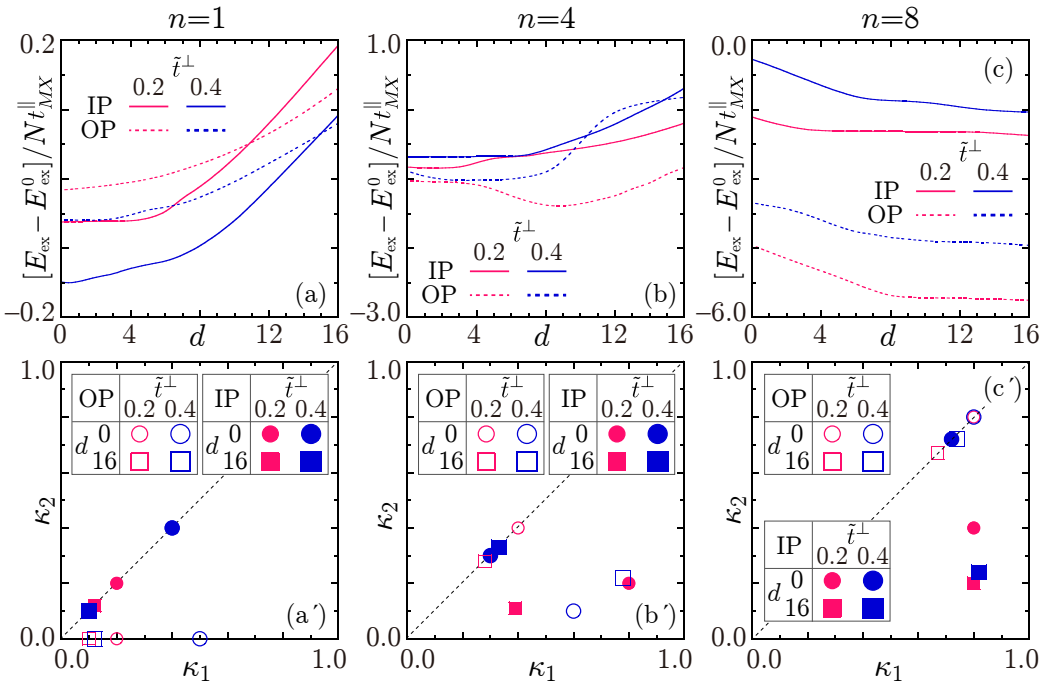

Figure 6. Adiabatic potential energy surfaces of the n-photon excited states [$n = 1$ (**a**); 4 (**b**); and 8 (**c**)] and the optimized $\kappa = (\kappa_1, \kappa_2)$ at $d = 0$ and 16 [$n = 1$ (**a′**); 4 (**b′**); and 8 (**c′**)] on the IP-CDW and OP-CDW backgrounds, where $\tilde{t}^{\perp} \equiv t^{\perp}_{MM}/t^{\parallel}_{MX}$.

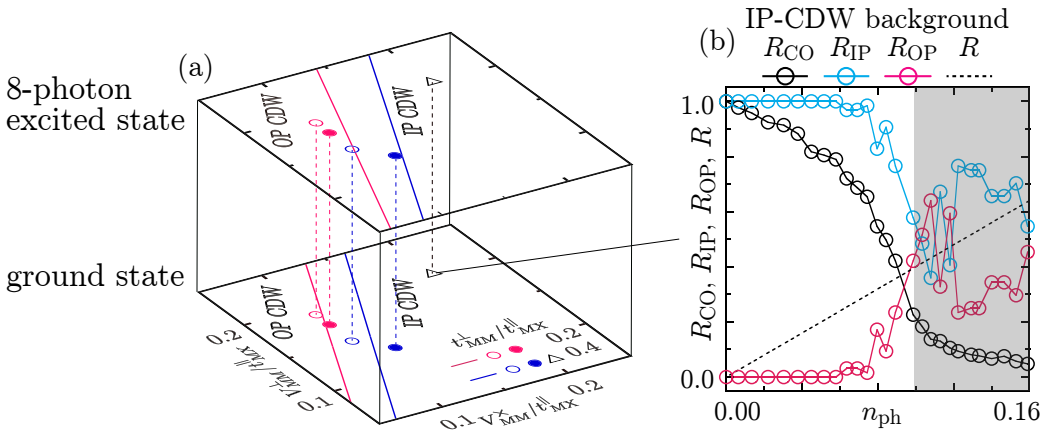

Figure 7. (**a**) Competition between OP CDW and IP CDW in the ground and photoexcited states. (**b**) The same as Figure 5 with another initial state (△).

5. Summary and Discussion

We have investigated photomanipulation of the IP-CDW and OP-CDW states in platinum-halide ladders. The Coulomb correlations $V^{\perp}_{MM}$ and $V^{\times}_{MM}$ favor OP CDW and IP CDW, respectively. The transfer integral $t^{\perp}_{MM}$ stabilizes the OP-type valence arrangement and this effect becomes more important in the photoexcited states. Weakening of the CDW order leads to a decrease in the Coulomb energy difference between IP CDW and OP CDW, and therefore the OP-type valence arrangement may become dominant in photoexcited states by the energy gain by $t^{\perp}_{MM}$. Thus, the photoinduced phase transition from IP CDW to OP CDW is possible, whereas the reverse process hardly occurs.

In photoexcited states, $4n_{\rm ph}$ electrons and $4n_{\rm ph}$ holes are simultaneously doped in a unit as carriers, where each carrier density is given by $n_{\rm ph}/2$. From the view point of carrier doping, we here compare the photodoping effect with the chemical doping effect on the electronic structures. In Figure 8a, we show the periodicity along the legs of the initial IP CDW at $t=-\infty$ and the photoinduced OP CDW with $n_{\rm ph}=0.1$ (carrier density is 0.05) at $t=2.9$ (ps), where the Fourier component of an electron density is defined as

$$F(t;q)=\frac{\sum_{l=1}^{2}\left|\sum_{n=1}^{N}e^{iqna}d_{n:l}(t)\right|}{\sum_{q}\sum_{l=1}^{2}\left|\sum_{n=1}^{N}e^{iqna}d_{n:l}(t)\right|}. \tag{36}$$

The initial sharp peak at $q=\pi/a$, which indicates the double periodicity, is smeared out by photoirradiation. This corresponds to a simple weakening of the background CDW order, as discussed in Figure 5. We further consider a mixture of the static ground states under the electron occupancy $\nu=0.8\,(=3/4+0.05=\nu_{\rm e})$ and $\nu=0.7\,(=3/4-0.05=\nu_{\rm h})$, which correspond to electron doping and hole doping, respectively, where the carrier density is 0.05 in each case. The Fourier component in the mixed state is estimated as

$$\bar{F}(q)=\{F(-\infty,q)|_{\nu=\nu_{\rm e}}+F(-\infty,q)|_{\nu=\nu_{\rm h}}\}/2. \tag{37}$$

This is shown in Figure 8b. $\bar{F}(q)$ has the multi-peaked structure due to the electron occupancy ν moving away from 3/4. The mixed state exhibits the multi-q CDW. Thus, the chemical doping breaks the initial double periodicity, whereas the photodoping can tune the only interchain valence arrangement. We note that such a contrast may depend on the lattice geometry: tubular analog compounds, such as the three-legged and four-legged MX tubes [51,52], show the persistent π-modulated Peierls distortion under chemical doping.

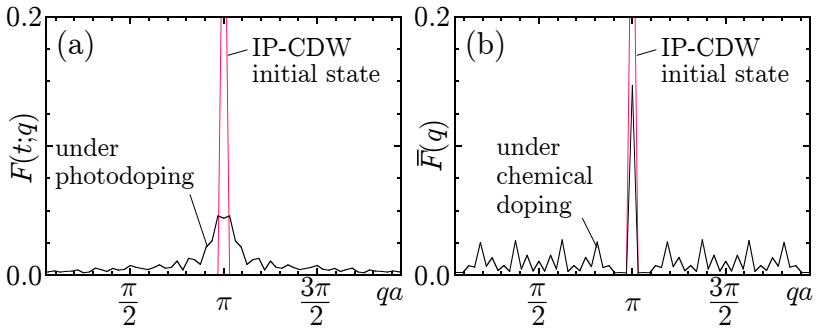

Figure 8. A carrier doping effect on the IP-CDW state at $t^{\perp}_{MM}/t^{\parallel}_{MX}=0.4$: a Fourier component of the electron density under photodoping (**a**) and that under chemical doping (**b**) are presented.

PtX ladder compounds with new interchain ligands have been recently synthesized [53]. A systematic investigation of the $t^{\perp}_{MM}$ effects is expected. In addition, recent optical observation in MX chains can reveal their light intensity dependences up to $\chi_{\rm ph}=0.5$ from $\chi_{\rm ph}=0.001$ ($\chi_{\rm ph}$: the

absorbed photon per metal site) [54]. Such optical measurement possibly detects the photoinduced directional phase transition in the platinum-halide ladder compounds.

Author Contributions: Calculation, Analysis, Writing, J.O. Calculation, Analysis, Writing, S.Y.

Funding: This work was supported by the Ministry of Education, Culture, Sports, Science and Technology of Japan.

Acknowledgments: The authors are grateful to I. Katayama and J. Takade for fruitful discussion.

Conflicts of Interest: The authors declare no conflict of interest.

References

1. Gammel, J.T.; Saxena, A.; Batistić, I.; Bishop, A.R. Two-band model for halogen-bridged mixed-valence transition-metal complexes. I. Ground state and excitation spectrum. *Phys. Rev. B* **1992**, *45*, 6408–6434. [CrossRef]
2. Weber-Milbrodt, S.M.; Gammel, J.T.; Bishop, A.R.; Loh, E.Y., Jr. Two-band model for halogen-bridged mixed-valence transition-metal complexes. II. Electron-electron correlations and quantum phonons. *Phys. Rev. B* **1992**, *45*, 6435–6458. [CrossRef]
3. Nasu, K. Extended Peierls–Hubbard Model for One-Dimensional N-Sites N-Electrons System. I. Phase Diagram by Mean Field Theory. *J. Phys. Soc. Jpn.* **1983**, *52*, 3865–3873. [CrossRef]
4. Bellitto, C.; Flamini, A.; Gastaldi, L.; Scaramuzza, L. Halogen Oxidation of Tetrakis(dithioacetato)diplatinum(II) Complexes, $Pt_2(CH_3CS_2)_4$. Synthesis and Characterization of $Pt_2(CH_3CS_2)_4X_2$ (X = Cl, Br, I) and Structural, Electrical, and Optical Properties of Linear-Chain (μ-Iodo)tetrakis(dithioacetato)diplatinum, $Pt_2(CH_3CS_2)_4I$. *Inorg. Chem.* **1983**, *22*, 444–449.
5. Kawakami, D.; Yamashita, M.; Matsunaga, S.; Takaishi, S.; Kajiwara, T.; Miyasaka, H.; Sugiura, K.; Matsuzaki, H.; Okamoto, H.; Wakabayashi, Y.; et al. Halogen-Bridged Pt^{II}/Pt^{IV} Mixed-Valence Ladder Compounds. *Angew. Chem.* **2006**, *118*, 7372–7375. [CrossRef]
6. Kobayashi, A.; Kitagawa, H. Mixed-Valence Two-Legged MX-Ladder Complex with a Pair of Out-of-Phase Charge-Density Waves. *J. Am. Chem. Soc.* **2006**, *128*, 12066–12067. [CrossRef] [PubMed]
7. Otsubo, K.; Wakabayashi, Y.; Ohara, J.; Yamamoto, S.; Matsuzaki, H.; Okamoto, H.; Nitta, K.; Uruga, T.; Kitagawa, H. Bottom-up realization of a porous metal-organic nanotubular assembly. *Nat. Mater.* **2011**, *10*, 291–295. [CrossRef] [PubMed]
8. Otake, K.; Otsubo, K.; Sugimoto, K.; Fujiwara, A.; Kitagawa, H. Ultrafine Metal-Organic Right Square Prism Shaped Nanowires. *Angew. Chem. Int. Ed.* **2016**, *55*, 6448–6451. [CrossRef] [PubMed]
9. Wada, Y.; Mitani, T.; Yamashita, M.; Koda, T. Charge Transfer Exciton in Halogen-Bridged Mixed-Valent Pt and Pd Complexes: Analysis Based on the Peierls–Hubbard Model. *J. Phys. Soc. Jpn.* **1985**, *54*, 3143–3153. [CrossRef]
10. Okamoto, H.; Toriumi, K.; Mitani, T. Optical and magnetic properties of the halogen-bridged metal complexes modified by hydrogen bondings: $\{M(1R, 2R\text{-cyclohexanediamine})_2Br\}Br_2$ (M =Pt, Pd, and Ni). *Phys. Rev. B* **1990**, *42*, 10381–10387. [CrossRef]
11. Toftlund, H.; Simonsen, O. Preparation and Structure of a New Kind of an Extended Partially Oxidized Linear-Chain Compound: catena-(μ-Bromo)bis((1*R*, 2*R*)-cyclohexanediamine)nickel(2.77) Bromide. *Inorg. Chem.* **1984**, *23*, 4261–4265. [CrossRef]
12. Toriumi, K.; Wada, Y.; Mitani, T.; Bandow, S. Synthesis and Crystal Structure of a Novel One-Dimensional Halogen-Bridged Ni^{III}-X-Ni^{III} Compound,$\{[Ni(R, R\text{-chxn})_2Br]Br_2\}_\infty$. *J. Am. Chem. Soc.* **1989**, *111*, 2341–2344. [CrossRef]
13. Sakai, M.; Kuroda, N.; Nishina, Y. Optical studies of the quasi-one-dimensional charge-density-wave state in $[Pt(en)_2][Pt(en)_2Cl_2](ClO_4)_4$ (en = ethylenediamine) under hydrostatic pressure. *Phys. Rev. B* **1989**, *40*, 3066–3076. [CrossRef]
14. Tanaka, H.; Hasegawa, Y.; Ito, H.; Kuroda, S.; Yamashita, T.; Mitsumi, M.; Toriumi, K. Control of the electronic phase transition of the MMX-chain complex $Pt_2(n\text{-pentylCS}_2)_4I$ with the uniaxial compression. *Synth. Met.* **2005**, *152*, 141–144. [CrossRef]

15. Kobayashi, A.; Tokunaga, A.; Ikeda, R.; Sagayama, H.; Wakabayashi, Y.; Sawa, H.; Hedo, M.; Uwatoko, Y.; Kitagawa, H. Pressure-Induced Metal-Semiconductor-Metal Transitions in an MMX-Chain Complex, $Pt_2(C_2H_5CS_2)_4I$. *Eur. J. Inorg. Chem.* **2006**, *2006*, 3567–3570. [CrossRef]
16. Kurmoo, M.; Clark, R.J.H. Spectroscopic Studies on Linear-Chain Semiconductors and Related Species. Vibrational and Resonance Raman Spectroscopy of the Diphosphite Complexes $K_4[Pt_2(pop)_4]\cdot 2H_2O$, $K_4[Pt_2(pop)_4X_2]\cdot 2H_2O$, and $K_4[Pt_2(pop)_4X]\cdot nH_2O$, X= Cl, Br, I. *Inorg. Chem.* **1985**, *24*, 4420–4425. [CrossRef]
17. Kimura, N.; Ohki, H.; Ikeda, R.; Yamashita, M. Valence structure of one-dimensional halogen bridged -Pt-Pt-X-Pt-Pt-X- type complexes studied by ^{31}P solid NMR. *Chem. Phys. Lett.* **1994**, *220*, 40–45. [CrossRef]
18. Kitagawa, H.; Onodera, N.; Sonoyama, T.; Yamamoto, M.; Fukawa, T.; Mitani, T.; Seto, M.; Maeda, Y. Charge Ordering with Lattice Distortions in a Conductive MMX-Chain Complex, $Pt_2(dta)_4I$ (dta=$CH_3CS_2^-$). *J. Am. Chem. Soc.* **1999**, *121*, 10068–10080. [CrossRef]
19. Swanson, B.I.; Stroud, M.A.; Conradson, S.D.; Zietlow, M.H. Observation of a Pressure Induced Reverse Peierls Instability in the Quasi-One-Dimensional Mixed Valence Solid $K_4[Pt_2(P_2O_5H_2)_4Br]\cdot 3H_2O$. *Solid State Commun.* **1988**, *65*, 1405–1409. [CrossRef]
20. Yamamoto, S. Pressure-induced phase transitions of halogen-bridged binuclear metal complexes $R_4[Pt_2(P_2O_5H_2)_4X]\cdot nH_2O$. *Phys. Rev. B* **2001**, *64*, 140102. [CrossRef]
21. Iwano, K. Theory for photoinduced phase transition from a charge-density-wave state to a Mott–Hubbard insulator in a quasi-one-dimensional Br-bridged Pd compound. *Phys. Rev. B* **2004**, *70*, 241102. [CrossRef]
22. Matsuzaki, H.; Yamashita, M.; Okamoto, H. Ultrafast Photoconversion from Charge Density Wave State to Mott–Hubbard State in One-Dimensional Extended Peierls–Hubbard System of Br-Bridged Pd Compound. *J. Phys. Soc. Jpn.* **2006**, *75*, 123701. [CrossRef]
23. Matsuzaki, H.; Matsuoka, T.; Kishida, H.; Takizawa, K.; Miyasaka, H.; Sugiura, K.; Yamashita, M.; Okamoto, H. Novel Optical and Magnetic Bistability and Photoinduced Transition in a One-Dimensional Halogen-Bridged Binuclear Pt Complex. *Phys. Rev. Lett.* **2003**, *90*, 046401. [CrossRef] [PubMed]
24. Yonemitsu, K.; Miyashita, N. Coherence recovery and photoinduced phase transitions in one-dimensional halogen-bridged binuclear platinum complexes. *Phys. Rev. B* **2003**, *68*, 075113. [CrossRef]
25. Kurita, S.; Haruki, M.; Miyagawa, K. Photo-Induced Defect States in a Quasi One-Dimensional Mixed-Valence Platinum Complex. *J. Phys. Soc. Jpn.* **1988**, *57*, 1789–1796. [CrossRef]
26. Kimura, K.; Matsuzaki, H.; Takaishi, S.; Yamashita, M.; Okamoto, H. Ultrafast photoinduced transitions in charge density wave, Mott insulator, and metallic phases of an iodine-bridged platinum compound. *Phys. Rev. B* **2009**, *79*, 075116. [CrossRef]
27. Funase, K.; Yamamoto, S. Competing Ground States of Metal-Halide Ladders. *J. Phys. Soc. Jpn.* **2006**, *75*, 044717. [CrossRef]
28. Iwano, K.; Shimoi, Y. Density Functional Theory of Chlorine-Bridged Platinum Complexes: Monomer, Chain, and Two-Leg Ladders. *J. Phys. Soc. Jpn.* **2007**, *76*, 063708. [CrossRef]
29. Yamamoto, S.; Ohara, J. Optical characterization of platinum-halide ladder compounds. *Phys. Rev. B* **2007**, *76*, 235116. [CrossRef]
30. Suemoto, T.; Nakao, H.; Nakajima, M.; Kitagawa, H. Time-resolved luminescence spectroscopy of self-trapped excitons in ladder type Br-bridged Pt complexes. *J. Chem. Phys.* **2011**, *134*, 224503. [CrossRef] [PubMed]
31. Yamamoto, S.; Ohara, J. Optical observations of new halogen-bridged platinum complexes assembled within a ladder lattice. *J. Matter. Sci. Mater. Electron.* **2009**, *20*, 367–370. [CrossRef]
32. Yonemitsu, K.; Nasu, K. Theory of photoinduced phase transitions in itinerant electron systems. *Phys. Rep.* **2008**, *465*, 1–60. [CrossRef]
33. Iwano, K. Precursor of photoinduced structural phase transitions in a coupled-chain system with an electron-lattice interaction. *Phys. Rev. B* **2001**, *65*, 024302. [CrossRef]
34. Hirano, Y.; Ono, Y. Photogeneration Dynamics of Nonlinear Excitations in Polyacetylene. *J. Phys. Soc. Jpn.* **2000**, *69*, 2131–2144. [CrossRef]
35. Bonche, P.; Koonin, S.; Negele, J.W. One-dimensional nuclear dynamics in the time-dependent Hartree-Fock approximation. *Phys. Rev. C* **1976**, *13*, 1226–1258. [CrossRef]
36. Terai, A.; Ono, Y. Solitons and Their Dynamics in One-Dimensional SDW Systems. *Prog. Theor. Phys. Suppl.* **1993**, *113*, 177–190. [CrossRef]

37. De Filippis, G.; Cataudella, V.; Nowadnic, E.A.; Devereaux, T.P.; Mishchenko, A.S.; Nagaosa, N. Quantum Dynamics of the Hubbard-Holstein Model in Equilibrium and Nonequilibrium: Application to Pump-Probe Phenomena. *Phys. Rev. Lett.* **2012**, *109*, 176402. [CrossRef] [PubMed]
38. Suzuki, M. General Decomposition Theory of Ordered Exponentials. *Proc. Jpn. Acad. Ser. B* **1993**, *69*, 161–166. [CrossRef]
39. Tanaka, Y.; Yonemitsu, K. Growth Dynamics of Photoinduced Domains in Two-Dimensional Charge-Ordered Conductors Depending on Stabilization Mechanisms. *J. Phys. Soc. Jpn.* **2010**, *79*, 024712. [CrossRef]
40. Koshibae, W.; Furukawa, N.; Nagaosa, N. Real-Time Quantum Dynamics of Interacting Electrons: Self-Organized Nanoscale Structure in a Spin-Electron Coupled System. *Phys. Rev. Lett.* **2009**, *103*, 266402. [CrossRef] [PubMed]
41. Yamamoto, S.; Ohara, J. Photoproduction of spin and charge carriers in halogen-bridged binuclear platinum chain complexes. *J. Phys. Condens. Matter* **2008**, *20*, 415215. [CrossRef]
42. Mishima, A.; Nasu, K. Nonlinear lattice relaxation of photogenerated charge-transfer excitation in halogen-bridged mixed-valence metal complexes. I. Soliton and self-trapped exciton. *Phys. Rev. B* **1989**, *39*, 5758–5762. [CrossRef]
43. Mishima, A.; Nasu, K. Nonlinear lattice relaxation of photogenerated charge-transfer excitation in halogen-bridged mixed-valence metal complexes. II. Polaron channel. *Phys. Rev. B* **1989**, *39*, 5763–5766. [CrossRef]
44. Baeriswly, D.; Bishop, A.R. Localised polaronic states in mixed-valence linear chain complexes. *J. Phys. C Solid State Phys.* **1988**, *21*, 339–356. [CrossRef]
45. Okamoto, H.; Mitani, T.; Toriumi, K.; Yamashita, M. Photogeneration of Solitons and Polarons in 1-D Halogen-Bridged Metal Complexes. *Phys. Rev. Lett.* **1992**, *69*, 2248–2251. [CrossRef] [PubMed]
46. Onodera, Y. Soliton Model for Halogen-Bridged Mixed-Valence Platinum Complexes. *J. Phys. Soc. Jpn.* **1987**, *56*, 250–254. [CrossRef]
47. Kuroda, N.; Sakai, M.; Nishina, Y.; Tanaka, M.; Kurita, S. Soliton-to-Band Optical Absorption in a Quasi One-Dimensional Pt^{II}-Pt^{IV} Mixed-Valence Complex under Hydrostatic Pressure. *Phys. Rev. Lett.* **1987**, *58*, 2122–2125. [CrossRef] [PubMed]
48. Koshino, K.; Ogawa, T. Domino Effects in Photoinduced Structural Change in One-Dimensional Systems. *J. Phys. Soc. Jpn.* **1998**, *67*, 2174–2177. [CrossRef]
49. Yonemitsu, K.; Nasu, K. Theory of Photoinduced Phase Transitions. *J. Phys. Soc. Jpn.* **2006**, *75*, 011008. [CrossRef]
50. Iwano, K. Mechanism for photoinduced structural phase transitions in low-dimensional electron-lattice systems: Nonlinearity with respect to excitation density and aggregation of excited domains. *Phys. Rev. B* **2000**, *61*, 279–289. [CrossRef]
51. Yamamoto, S.; Ohara, J.; Ozaki, M. Ground-State Properties of a Peierls–Hubbard Triangular Prism. *J. Phys. Soc. Jpn.* **2010**, *79*, 044709. [CrossRef]
52. Yamamoto, S.; Ohara, J. Competing ground states of a Peierls–Hubbard nanotube. *Europhys. Lett.* **2009**, *87*, 17006.
53. Otsubo, K.; Kobayashi, A.; Sugimoto, K.; Fujiwara, A.; Kitagawa, H. Variable-Rung Design for a Mixed-Valence Two-Legged Ladder System Situated in a Dimensional Crossover Region. *Inorg. Chem.* **2014**, *53*, 1229–1240. [CrossRef] [PubMed]
54. Iwai, S.; Ono, M.; Maeda, A.; Matsuzaki, H.; Kishida, H.; Okamoto, H.; Tokura, Y. Ultrafast Optical Switching to a Metallic State by Photoinduced Mott Transition in a Halogen-Bridged Nickel-Chain Compound. *Phys. Rev. Lett.* **2003**, *91*, 057401. [CrossRef] [PubMed]